Geophysical Journal International

Estimation of *in-situ* horizontal stresses based on multiscale borehole breakout data via machine learning: model development, validation and application

Zizhuo Xiang [1,2] Won-Hee Kang,[3] Yinlin Ji,[4,5] Guangyao Si,[1] Ismet Canbulat,[1] Huasheng Lin[6] and Joung Oh [1]

[1] *School of Minerals and Energy Resources Engineering, University of New South Wales, Sydney, NSW* 2052*, Australia. E-mail:* joung.oh@unsw.edu.au
[2] *School of Physics, Chemistry and Earth Sciences, The University of Adelaide, Adelaide, SA* 5005*, Australia*
[3] *Centre for Infrastructure Engineering, School of Engineering, Design and Built Environment, Western Sydney University, Penrith, NSW* 2751*, Australia*
[4] *Helmholtz Centre Potsdam GFZ German Research Centre for Geosciences, Telegrafenberg,* D-14473 *Potsdam, Germany*
[5] *School of Earth Sciences and Engineering, Nanjing University, Nanjing* 210023*, China*
[6] *Blackwater Mine, Whitehaven Coal, Blackwater, QLD* 4717*, Australia.*

SUMMARY

Borehole breakout (BO) has increasingly been utilized to estimate *in-situ* stress magnitudes given the importance of the stress field in subsurface activities and the limitations of conventional stress measurement techniques. In this study, a new backpropagation neural network model is developed to estimate both maximum and minimum horizontal stress magnitudes from multiscale BO data. A total of 150 experimental data points from pre-stressed true-triaxial laboratory tests and 44 field data from a mine site in Australia and the literature are collected and employed for model development and validation. Compared to previous studies, the collected data set is significantly enhanced in both quantity and quality. To address discrepancies in stress magnitudes between experimental and field data, the three principal stresses are normalized by borehole wall strength (BWS). Overall, the model achieves mean absolute percentage errors of below 8 per cent for the maximum horizontal stress and below 20 per cent for the minimum horizontal stress, significantly outperforming the previous model developed for this purpose. Furthermore, these error rates fall within the typical error range (10–20 per cent) of conventional stress measurement techniques, indicating the model's sufficient accuracy for practical applications. Moreover, the effectiveness and generalizability of the model are verified using 166 additional BOs from two mine sites, which are independent of those used in model development. Continuous and detailed stress profiles are established based on these BOs, covering greater depth intervals than the stress measurements from the overcoring method. The results of this study demonstrate that the proposed model can provide reliable and accurate stress estimation, utilizing input parameters that can be readily obtained from borehole geophysical logs.

Key words: Machine learning; Neural networks, fuzzy logic; Downhole methods; Geomechanics.

1 INTRODUCTION

Knowledge of the *in-situ* stress field is crucial for a wide range of subsurface activities, including for example, mining and petroleum operations, carbon geosequestration, hydrogen storage and geothermal energy production. Common *in-situ* stress measurement techniques, such as overcoring, hydraulic fracturing, flat jack and acoustic methods (Kaiser effects), could effectively provide direct estimates of the stress field orientation and magnitude (Haimson &

Cornet, 2003; Lavrov, 2003; Sjöberg *et al.*, 2003; Figueiredo *et al.*, 2010; Lai *et al.*, 2019). However, they are generally cost-intensive and time-consuming due to the need for field or laboratory testing (Fairhurst, 2003; Ljunggren *et al.*, 2003). Furthermore, as these techniques often only offer a point measurement of the local stresses per test, extensive testing is required to establish a comprehensive understanding of the regional stress field.

Borehole breakout (BO) refers to symmetrical V-shaped elongations on opposite sides of the borehole walls, commonly observed in
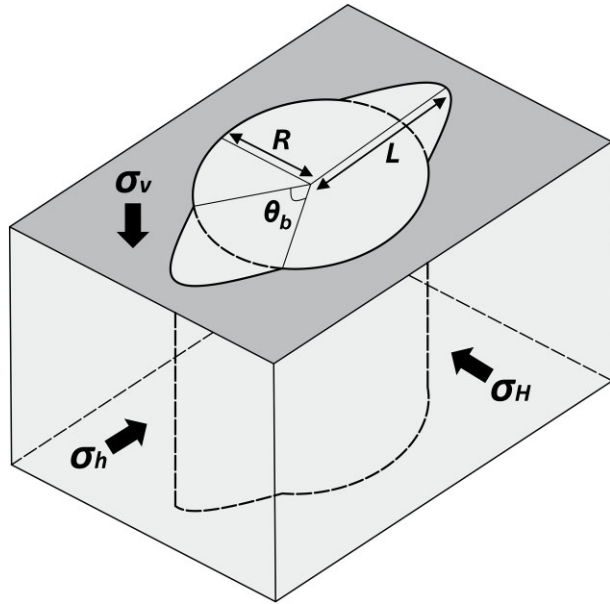
Figure 1. Schematic diagram of a V-shaped BO in a vertical borehole.

boreholes of various depths (Cox, 1972; Zoback *et al*., 1985; Lucier *et al*., 2009; Jo *et al*., 2019). The extent of BO can be characterized by two geometric parameters: angular span (θ_b) and BO depth (L) normalized by borehole radius (R) (L/R), as indicated in Fig. 1. In vertical boreholes, as the redistributed stress primarily concentrates along the minimum horizontal stress (σ_h) direction around the circumference, the BO azimuth has been broadly utilized as a robust indicator of stress orientations (Gough & Bell, 1981; Qian & Pedersen, 1991; Zhang *et al*., 1994; Borm *et al*., 1997). According to the latest World Stress Map data base, BO contributes up to 50 per cent of the stress orientation data within the upper 5 km of the Earth's crust, surpassing other indicators such as earthquake focal mechanisms, drilling-induced tensile fractures and hydraulic fracturing (Heidbach *et al*., 2018). Furthermore, attempts have been made to derive or constrain the horizontal stress magnitudes from BO geometries as an alternative to conventional stress measurement techniques. Analytical methods, such as those described in Barton *et al*. (1988) and Zoback *et al*. (2003), correlate the redistributed stress around the BO boundaries with the strength of the rock to constrain the stress range or calculate the maximum horizontal stress (σ_H) from σ_h. Numerical methods have also been adopted by iteratively varying boundary stresses to match numerical BO shapes with observed field data (Shen, 2008; Kim *et al*., 2017). Although these methods have demonstrated varying degrees of success in practical applications, they generally provide only the range and relative magnitudes of the horizontal stresses or require iterative computation for each data point.

Since the extent of BO is directly correlated with redistributed virgin stresses, machine learning regression models have been increasingly adopted in recent years to estimate explicit stress magnitudes from BO geometries. Compared with the analytical and numerical approaches mentioned previously, machine learning methods can provide relatively higher estimation accuracy given their ability to capture nonlinear correlations between input features and target outputs, as demonstrated in various geomechanical and geophysical applications (Bergen *et al*., 2019; W. Zhang *et al*., 2023). Zhang *et al*. (2018) developed a

backpropagation neural network (BPNN) for horizontal stress estimation based on a BO data base generated from finite element method (FEM) simulations, and the same methodology was later adopted by Zhang & Yin (2019) and Garavand & Hadavimoghaddam (2023). However, these numerically generated data sets were not calibrated or validated against real-world data, and the applicability of these models under field conditions was not verified. Lin, *et al*. (2020a, c) and Wu *et al*. (2024) compiled data sets consisting of 79 to 106 experimental data points and 19 to 23 field data points for the development of Kriging and BPNN models, which are considered more practical compared to those based on FEM data. Nonetheless, the reliability of these models remains significantly constrained by the quantity and quality of available data sets, particularly the lack of field data. Moreover, they were built either using only one BO geometry or to predict only one horizontal stress component, failing to consider that θ_b and L/R have different formation mechanisms and are affected by the combined effect of both horizontal stresses (Lee *et al*., 2016; Xiang *et al*., 2024b).

To address the aforementioned limitations, a new BPNN regression model is introduced in this study to estimate both σ_H and σ_h stress magnitudes from BO geometries. A new data set, comprising 194 experimental and field data points, is used for model development and validation. The effectiveness and generalizability of the model are further evaluated using additional field data from two mine sites in Australia. Compared with conventional stress measurement techniques, the inputs of the proposed model are primarily obtained from borehole geophysical logs without additional testing, as the logging data have often already been collected for other applications, such as mineral exploration and geological structure imaging. Furthermore, since BOs are commonly observed in boreholes, continuous stress profiles can be established using the proposed model, which can further contribute to the modelling of the regional stress field. The outcomes of this study are also expected to provide valuable data and new insights into the methodologies for developing stress estimation models from BOs using machine learning techniques.

2 DATA COLLECTION AND ANALYSIS

2.1. Experimental data

Given the difficulties in obtaining sufficient field data, experimental data are used to establish the primary data set for model development. Two common testing methodologies for studying BO are the pre-drilled (PD) method (applying true-triaxial stresses to specimens with pre-drilled boreholes) and the pre-stressed (PS) method (applying true-triaxial stresses to intact specimens and then conducting drilling). Based on *in-situ* observations, numerical simulations and systematic experimental investigations (Martin, 1997; Eberhardt, 2001; Xiang *et al*., 2024c), it is believed that the PS method more realistically reproduces BO formation under field conditions due to the impacts of stress path and removal of the rock debris by the drilling fluid and vibration. Therefore, to ensure the reliability of the model, only PS experimental data are collected for model development.

An example of the PS testing setup and procedures is given in Fig. 2. First, true-triaxial far-field stresses are applied to the rectangular prismatic samples and maintained for approximately 10–15 min to allow stabilization. The specimen size varies
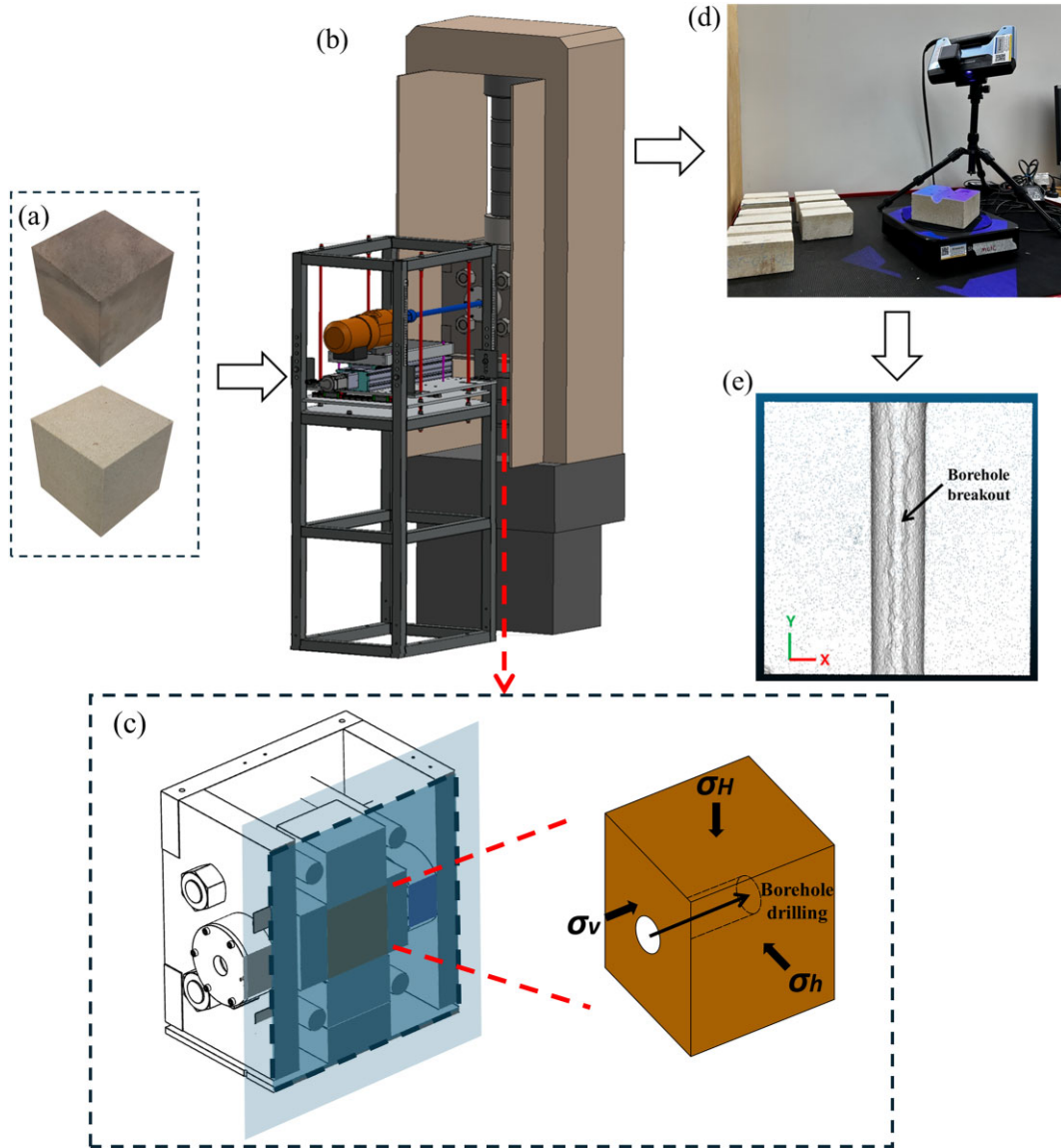
Figure 2. An example of the PS experimental setup and procedures (after Xiang et al., 2024b, 2024c). (a) Rectangular prismatic rock specimens; (b) True-triaxial PS BO experiment; (c) Schematic diagram showing the stress directions and borehole location on the specimen; (d) 3-D scanning of the tested specimens; (e) Scanned point cloud data of a tested specimen.

between $120 \times 120 \times 120$ mm^3, $127 \times 127 \times 178$ mm^3 and $153 \times 153 \times 229$ mm^3 (Haimson & Kovacich, 2003; Haimson, 2007; Xiang *et al.*, 2024c). Subsequently, drilling is carried out along the vertical stress (σ_v) direction, and fluid (tap water) is circulated through the drill bit and borehole to cool down the drill bit and remove BO debris. Upon completion of the drilling, the drill bit is retracted, and the same stress state is maintained for an additional 30 min to allow BO formation and stabilization. Post-experiment, the BO geometries are extracted through optical scanning.

Six sets of PS experimental data based on Gosford sandstone (Xiang *et al.*, 2024b), yellow mudstone (Xiang *et al.*, 2024b), Alabama limestone (Herrick & Haimson, 1994), Tablerock sandstone (Haimson & Lee, 2004), Tenino sandstone (Lee *et al.*, 2016) and Westerly granite (Song, 1998) are collected from the literature. Additionally, since the study by Xiang *et al.* (2024b), six new experiments have been conducted on Gosford sandstone and included in this study.

In total, the experimental data set comprises 150 PS data points across various rock types, representing a considerable improvement in both data quantity and consistency in the experimental approach compared with previous studies. These data are listed in Table A1 in Appendix A.

Due to the limitations of laboratory conditions, the diameter of the borehole for all experimental data is around 22 mm, which is smaller than those in the field. To incorporate the borehole size effect (Bažant *et al.*, 1993; Martin *et al.*, 1994; Dresen *et al.*, 2010; Papamichos, 2010; Lin *et al.*, 2020b), borehole wall strength (BWS) is commonly employed to replace uniaxial compressive strength (UCS) to represent the rock strength along the wall of relatively small boreholes, which can be calculated by eq. (1) (Lin *et al.*, 2021).

$$\text{BWS} = \left(0.0005R^2 - 0.0638R + 2.7885\right)\text{UCS}, \qquad (1)$$

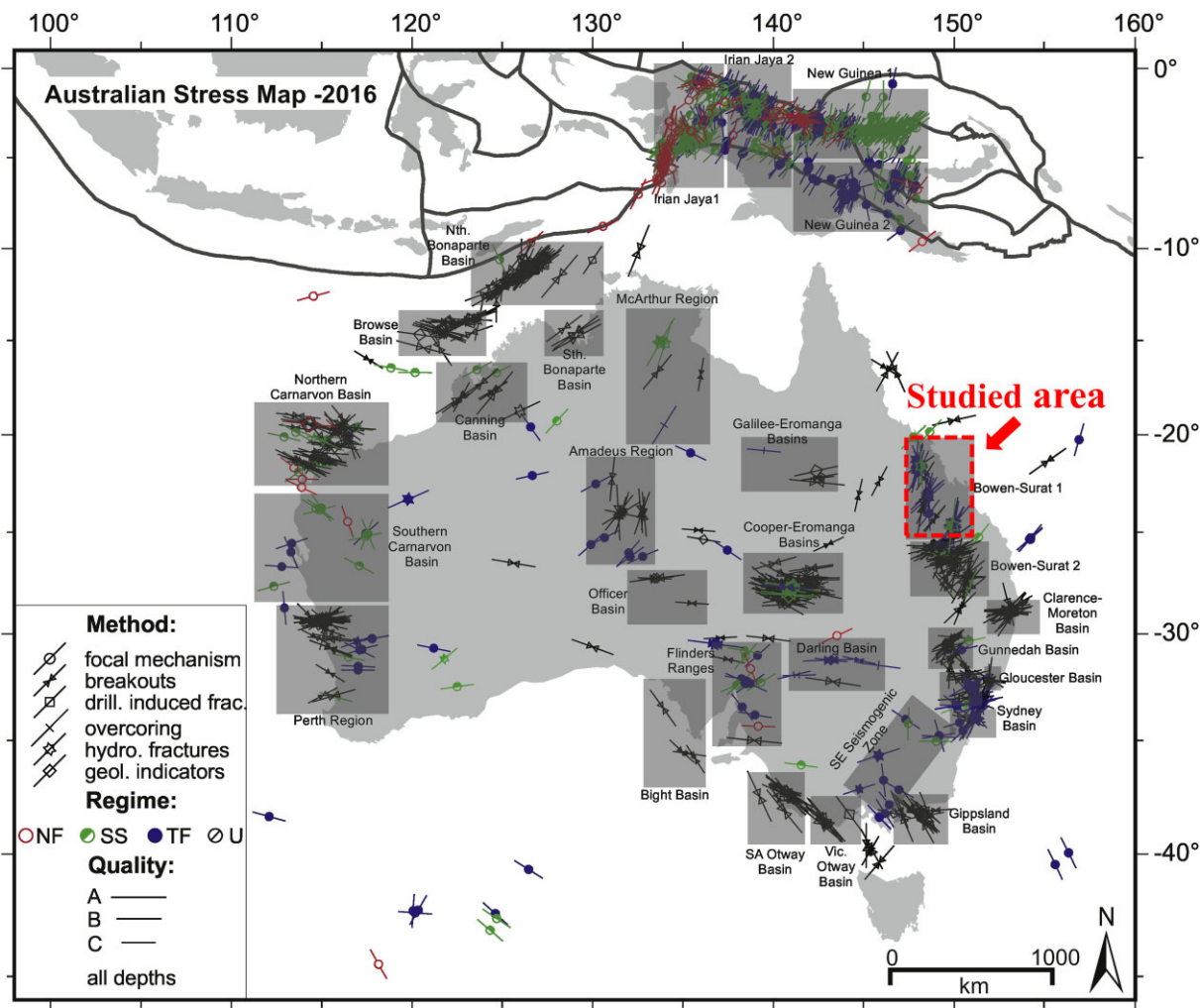where R represents the radius of the borehole in mm.

Figure 3. Location of the studied area (highlighted by the dashed box) (after Rajabi *et al.*, 2017). The grey regions represent the various stress provinces in Australia.

2.2. Field data

Field data is crucial for model development, representing real-world conditions and variability and essential for accurate model calibration and validation. The paucity of field data has always been a significant constraint in previous studies. To address this issue, a new set of field data is obtained from exploration boreholes of a coal mine (Mine A) located in the Bowen-Surat 1 area of the Bowen Basin, Queensland, Australia (Fig. 3). These exploration boreholes were drilled vertically from the surface to depths of around 300 to 600 m prior to mining. Extensive *in-situ* stress measurements were conducted at multiple boreholes through the overcoring method. According to these stress measurements and the World Stress Map data base (Rajabi *et al.*, 2017), the stress fields around the studied area are primarily under the thrust faulting (TF) stress regime ($\sigma_H > \sigma_h > \sigma_v$), with a small amount of data indicating a strike-slip (SS) stress regime ($\sigma_H > \sigma_v > \sigma_h$) (Anderson, 1905). The measured σ_H is primarily oriented towards 20° to 70° from magnetic north (NE-SW), which is consistent with the World Stress Map data at this region.

Geophysical logging was carried out in most exploration boreholes, including density, gamma, caliper, acoustic televiewer (ATV), sonic, neutron and verticality logs. The log analysis was performed using the commercially available software WellCAD™ 5.7

(Advanced Logic Technology, Luxembourg). Quality assurance and quality control (QAQC) were conducted by the field engineers and service providers to ensure the reliability of the logs. Borehole BOs are identified based on the ATV and caliper logs. As the maximum deviations of these exploration boreholes are generally smaller than 3°, the boreholes are assumed to be vertical and aligned with the σ_v direction. Therefore, the BO orientation is considered to correspond to the direction of σ_h. For BO geometry extraction, the traveltime from the ATV logs is first converted to the borehole radius, and the radius values at BO locations are then averaged along the length of the BO to reduce local noise. BO geometries are determined by comparing the borehole radius at BO locations with the radius of intact borehole sections adjacent to the BOs, and the final BO dimensions are obtained by averaging the values from both sides of the borehole. An example of an extracted BO and the averaged BO profile and cross-section are shown in Fig. 4. The extraction process is executed through a program written in Python, similar to that described in Wang *et al.* (2023). QAQC is carried out on the extracted BO data based on the following criteria:

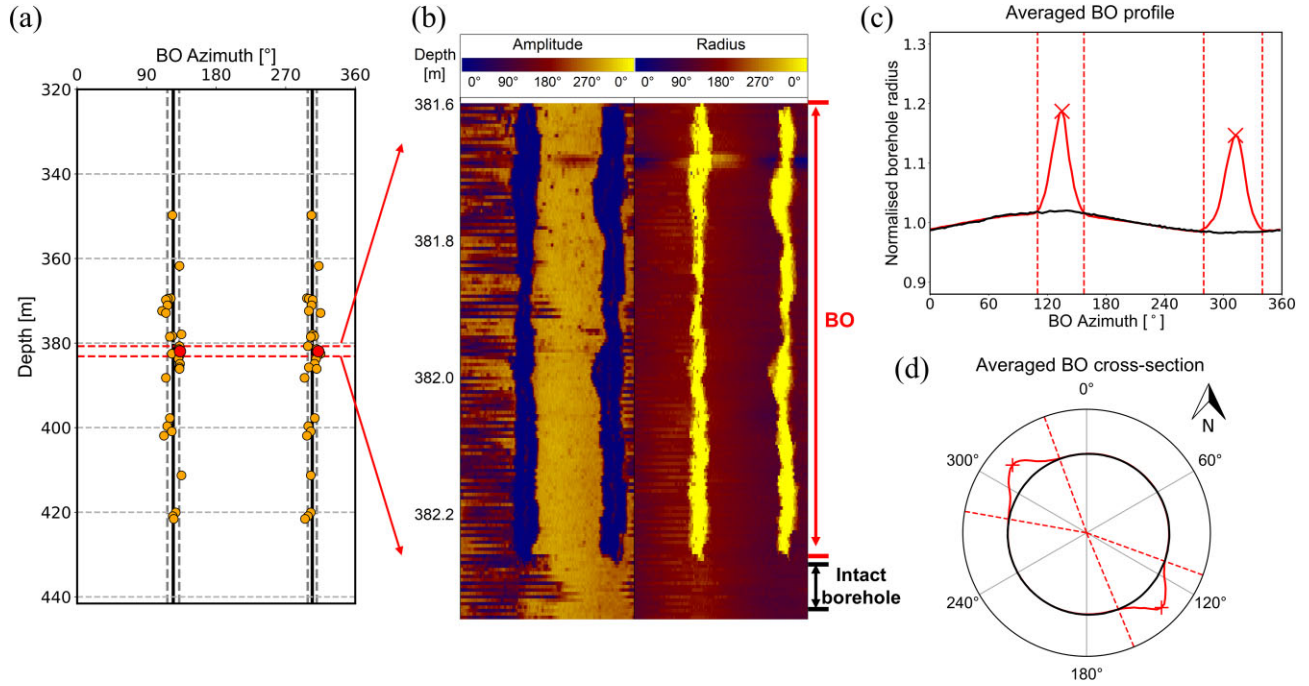(i) The BO is not intersected by geological structures (e.g. fractures) (LeRiche, 2017).

Figure 4. An example of an extracted BO. (a) Depth and orientation of observed BOs along an exploration borehole; (b) Acoustic image log of the BO at the depth of 381.6 to 382.3 m. The BO is denoted by the blue area in the amplitude log and the yellow area in the radius log (derived from the traveltime log); (c) Averaged BO profile along the length of the BO derived from the radius log; (d) Averaged BO cross-section derived from (c). In (c) and (d), the black line represents the radius of the intact borehole beneath the BO, the red solid line is the averaged radius at the BO location, the red dashed lines represent the BO boundaries and the red cross marks indicate the tips of the BO.

(ii) The difference in azimuths of BOs on both sides of the borehole is within $180° \pm 20°$ (Snee & Zoback, 2018; Wang & Schmitt, 2020).

(iii) The variations in θ_b and *L/R* of BOs on both sides of the borehole are within $20°$ and 0.1, respectively.

(iv) The BO has less than $0.75°\,\text{cm}^{-1}$ deviation (LeRiche, 2017).

In-situ horizontal stress measurements obtained through the overcoring method are paired with BO data from the same or nearby boreholes if the following conditions are met: the BO orientation is within $\pm10°$ of the measured σ_h direction, the vertical distance between the BO and stress measurement is within ±2 m, and both are located in the same strata. The σ_v magnitudes at BO locations are calculated based on the average unit weight of the overburden obtained from density logs (approximately $2450\,\text{kg}\,\text{m}^{-3}$ for the site of interest) and the depths of BOs. The rock UCS values are either obtained directly from laboratory tests on the core samples or estimated through the borehole geophysical logs. For the latter, five types of borehole geophysical logs (sonic velocity, gamma, neutron, porosity and density logs) are collected, and the models developed by Xiang *et al.* (2023c) are adopted to estimate the UCS values. Since the borehole diameters at BO locations are approximately 100 mm, BWS is assumed to be equal to the rock UCS value (Martin *et al.*, 1994; Martin, 1997; Qiao *et al.*, 2024). In total, 34 field data points are obtained from 16 boreholes following the above procedure for model development and validation, with depths ranging from 260 to 436 m. The measured horizontal stress orientations and magnitudes of these field data are exhibited in Fig. 5. The lithologies of these data points are primarily sandstone, siltstone and interbedded sandstone and siltstone.

Moreover, ten additional field data points are collected from two mine sites in Australia (Lin *et al.*, 2020a; Xiang *et al.*, 2024a),

KGHM's Victoria Project in Canada (LeRiche, 2017) and ACEL's Mine-by Experiment in Canada (Martin, 1997). These data points have been employed in past studies for stress estimation based on BO data and are included here to supplement the analysis and model development (Lin et al., 2020a, 2020c; Wu *et al.*, 2024). All collected field data are listed in Table A2 in Appendix A.

2.3. Data analysis

The distributions of the PS experimental data and field data are illustrated in Fig. 6. The common practice for estimating *in-situ* stresses based on BO data involves using one or two BO geometries, σ_v, and rock strength as input features to estimate σ_H and/or σ_h. In the collected data set, the distribution of θ_b follows a normal distribution pattern, with the peak frequency occurring at approximately $40°$ for the experimental data and $30°$ for the field data. *L/R* for both experimental and field data clusters towards the lower values between 1.0 and 1.3. The range of BO geometry values for the field data is generally aligned with those observed from deeper wellbores, with depths ranging from 900 m to 3.5 km (Vernik & Zoback, 1992; Walton *et al.*, 2015; Pierdominici *et al.*, 2020), and tends to cluster towards relatively lower values compared to the experimental data. Nevertheless, the field BO geometry values remain within the range of the experimental data. On the other hand, due to the high BWS values resulting from the borehole size effect, considerably higher stress magnitudes were used in laboratory experiments to induce BO. These experimental stress values, especially the high σ_H, may not represent the typical stress magnitudes observed in field conditions. Consequently, significant discrepancies can be found in the value ranges of principal stresses and BWS between the collected experimental and field data, which are commonly ignored in past research. Models built solely from experimental data with these
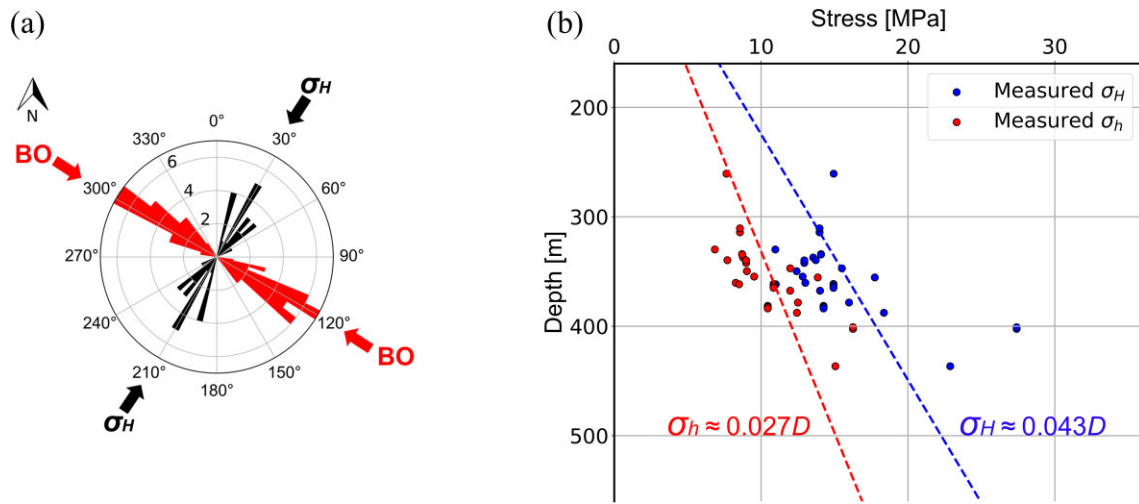
Figure 5. (a) Measured σ_H orientation relative to the BO directions. The radial axis represents the number of data; (b) Horizontal stress magnitudes of the collected field data. The blue and red dashed lines are the stress gradients obtained from measured σ_H and σ_h through linear fitting, respectively.
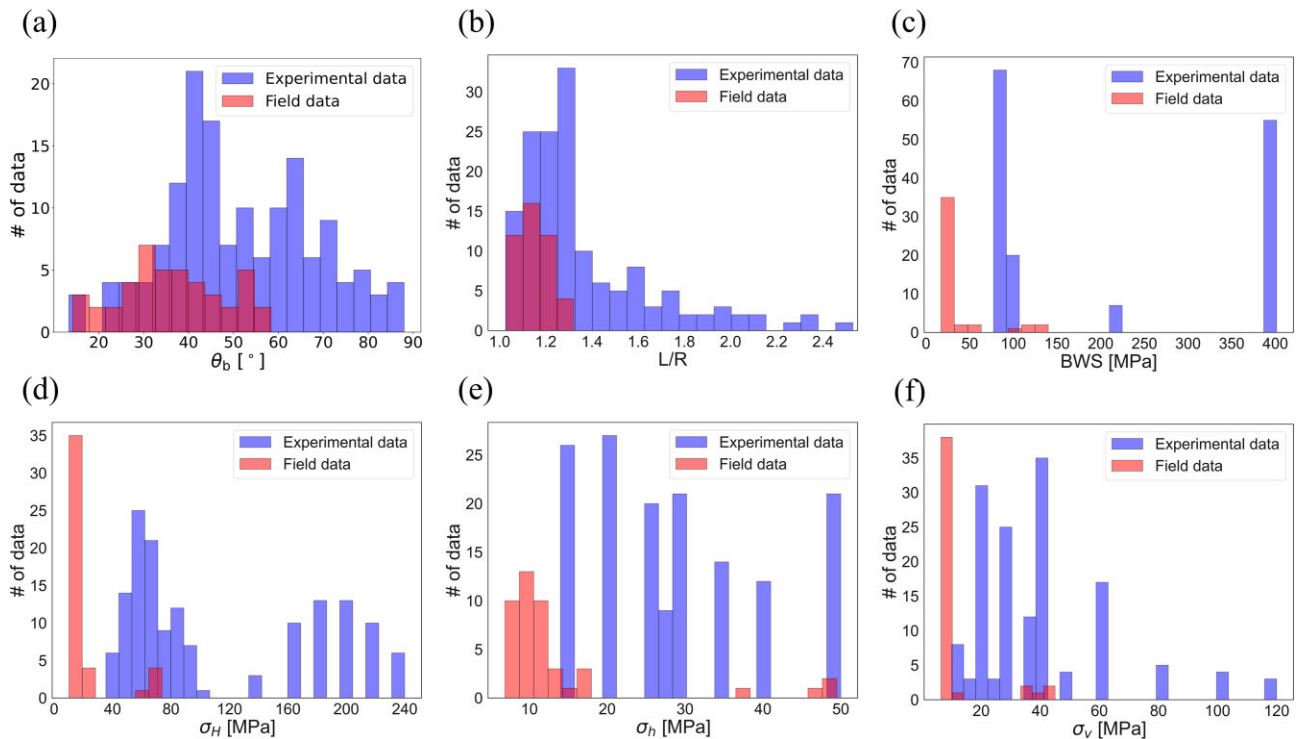

Figure 6. The distribution of the collected data: (a) θ_b; (b) L/R; (c) BWS; (d) σ_H; (e) σ_h; (f) σ_v.

high stress values may not yield accurate predictions of σ_H and σ_h magnitudes in field applications.

To address the aforementioned stress discrepancies and effectively utilize the experimental data, the principal stress magnitudes are normalized by BWS values. Both σ_H/BWS and σ_h/BWS are selected as the model target outputs, while σ_v/BWS, BWS and both BO geometries (i.e. θ_b and L/R) are utilized as the input parameters. The correlations and distributions of all variables are presented in Fig. 7. Overall, the normalized principal stresses (σ_H/BWS, σ_h/BWS and σ_v/BWS) in the experimental data demonstrate significantly improved consistencies with those of the field data, which is expected to enhance estimation reliability. σ_H/BWS exhibits relatively strong correlations with all input features, whereas σ_h/BWS shows a stronger correlation with σ_v/BWS and BWS but

significantly weaker correlations with θ_b and L/R. Note that due to the fixed testing material and borehole size, BWS remains the same within each subset of experimental data.

3 MODEL DEVELOPMENT AND RESULTS

3.1. Model development

Prominent machine learning regression algorithms include linear models, decision trees, ensemble regression models, support vector machines (SVM) and BPNN (Bergen *et al.*, 2019; Li *et al.*, 2022; Mahmoodzadeh *et al.*, 2022). A series of preliminary
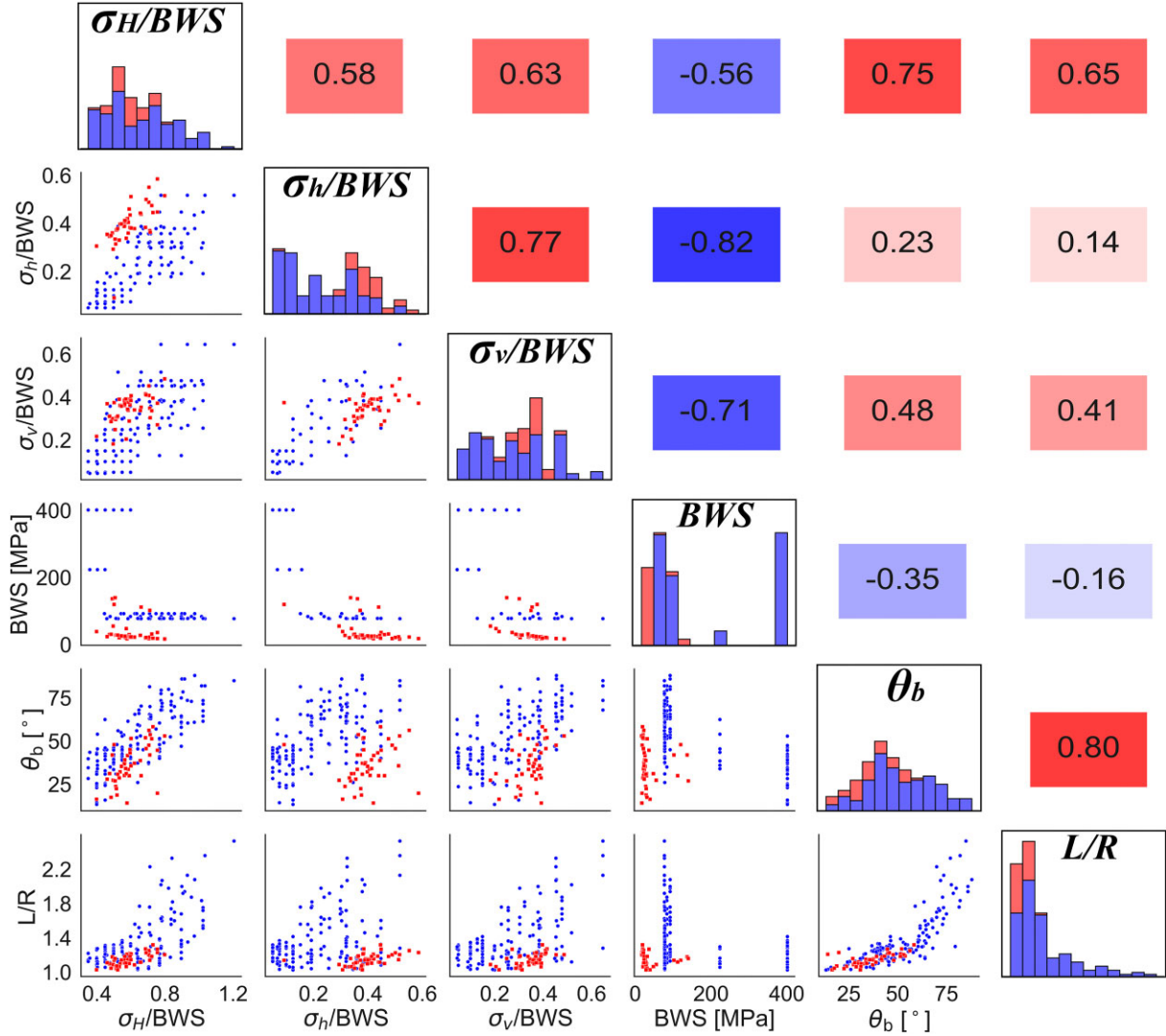
Figure 7. Pairwise scatter plot matrix, histograms and correlation coefficients of all variables used in the model. Pairwise scatter plots are displayed in the lower triangle boxes, with the experimental data represented by blue points and the field data by red points. Histograms are shown in the diagonal boxes, with the field data (red) stacked on top of the experimental data (blue). Correlation coefficients between each variable are given in the upper triangle boxes.

trials have been conducted to compare the performance of BPNN, SVM, random forest (RF) and eXtreme Gradient Boosting (XG-Boost) algorithms on the collected data set. The results indicate that the overall performance of these algorithms is similar, likely due to the relatively small data set size and the straightforward correlations between input parameters and output targets. Nonetheless, the BPNN algorithm exhibits slightly better accuracy and generalization in the collected field data. Furthermore, Lin *et al.* (2022) showed that the BPNN outperformed other algorithms in estimating σ_h from BO data. Therefore, BPNN is selected as the machine learning algorithm for this study.

The workflow for model development is depicted in Fig. 8. All experimental data and field data collected from the literature are employed for the BPNN model development, whereas the data from Mine A is randomly partitioned into two subsets, with 50 per cent used for development and the remaining 50 per cent reserved for model validation. The model development data set contains 177 experimental and field data points, which is then split into 75 per cent for training and 25 per cent for testing (Ceryan *et al.*, 2021; Furtney *et al.*, 2022). Data pre-processing involves

normalizing the stress values by BWS, as discussed in Section 2.3. Prior to training, the training data set is normalized through Z-score normalization. The hyperparameters of the BPNN, including the learning rate, the number of hidden layers, the number of neurons in each hidden layer and the optimizer, are tuned using the Tree-structured Parzen Estimator (TPE) optimization algorithm (Bergstra *et al.*, 2011). The PyTorch and Optuna libraries in the Python environment are adopted for model development and optimization. Model accuracy is evaluated based on two common performance measures: mean absolute percentage error (MAPE) and root mean squared errors (RMSE). The optimized model with the least MAPE and RMSE is saved and then applied to the remaining 50 per cent of the field data from Mine A to directly verify its performance.

3.2. Model results and validation

Following the workflow indicated in Fig. 8, the optimized BPNN contains two hidden layers, with 18 neurons in the first layer and 21 neurons in the second layer. Each hidden layer utilizes
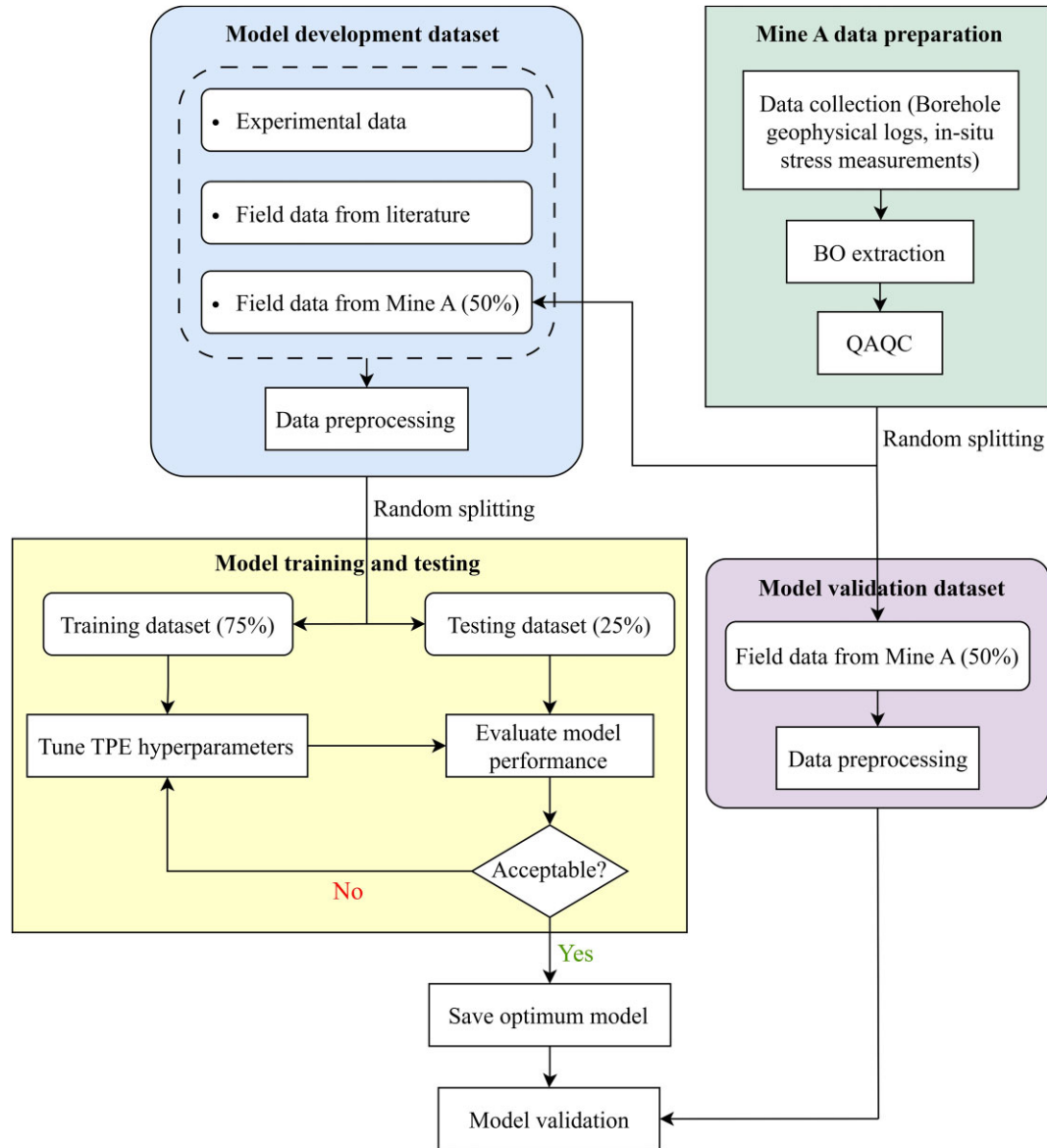
Figure 8. Workflow for BPNN model development.

the Rectified Linear Unit (ReLU) activation function. The model employs the mean-squared error (MSE) as the loss function and Adaptive Moment Estimation (Adam) as the optimizer. The results for the training, testing and validation data sets are exhibited in Fig. 9, and the accuracies of the estimated σ_H and σ_h are given in Table 1.

In general, both σ_H and σ_h are relatively accurately estimated by the model. For the model development data set, the model yields MAPE and RMSE of 7.96 per cent and 10.35 MPa for σ_H, respectively, while the corresponding values for σ_h are 19.62 per cent and 6.92 MPa. The errors associated with both horizontal stresses in the field data are generally smaller compared to those in the experimental data. In the validation data set, while some estimated values, especially σ_h/BWS (Fig. 9f), exhibit discrepancies compared to actual results, the estimation accuracies remain consistent with those of the model development data set. The MAPEs for σ_H and σ_h are 6.80 per cent and 12.49 per cent, respectively. The RMSEs are significantly improved compared to those of the development data

set, at 2.14 MPa for σ_H and 1.86 MPa for σ_h, due to the smaller horizontal stress magnitudes of the field data. The factors contributing to the accuracy difference between σ_H and σ_h and the overall model errors are discussed in Section 5. Given that the inherent errors associated with the overcoring *in-situ* stress measurement method range around 10–20 per cent (Amadei & Stephansson, 1997; Sjöberg & Klasson, 2003), the achieved estimation errors of around 8 per cent for σ_H and under 20 per cent for σ_h from borehole BOs suggest that the model is well-trained and sufficiently accurate for practical applications.

A comparison between the proposed model and the previous model developed by Lin *et al.* (2020c), which is also capable of estimating both horizontal stresses, is provided in Appendix B. In general, the proposed model considerably outperforms Lin's model in estimating both horizontal stresses, especially σ_h, across the entire data set. The improvement can be attributed to several factors. Firstly, this study utilizes a total of 177 experimental and field data points for model development, which is a significant improvement
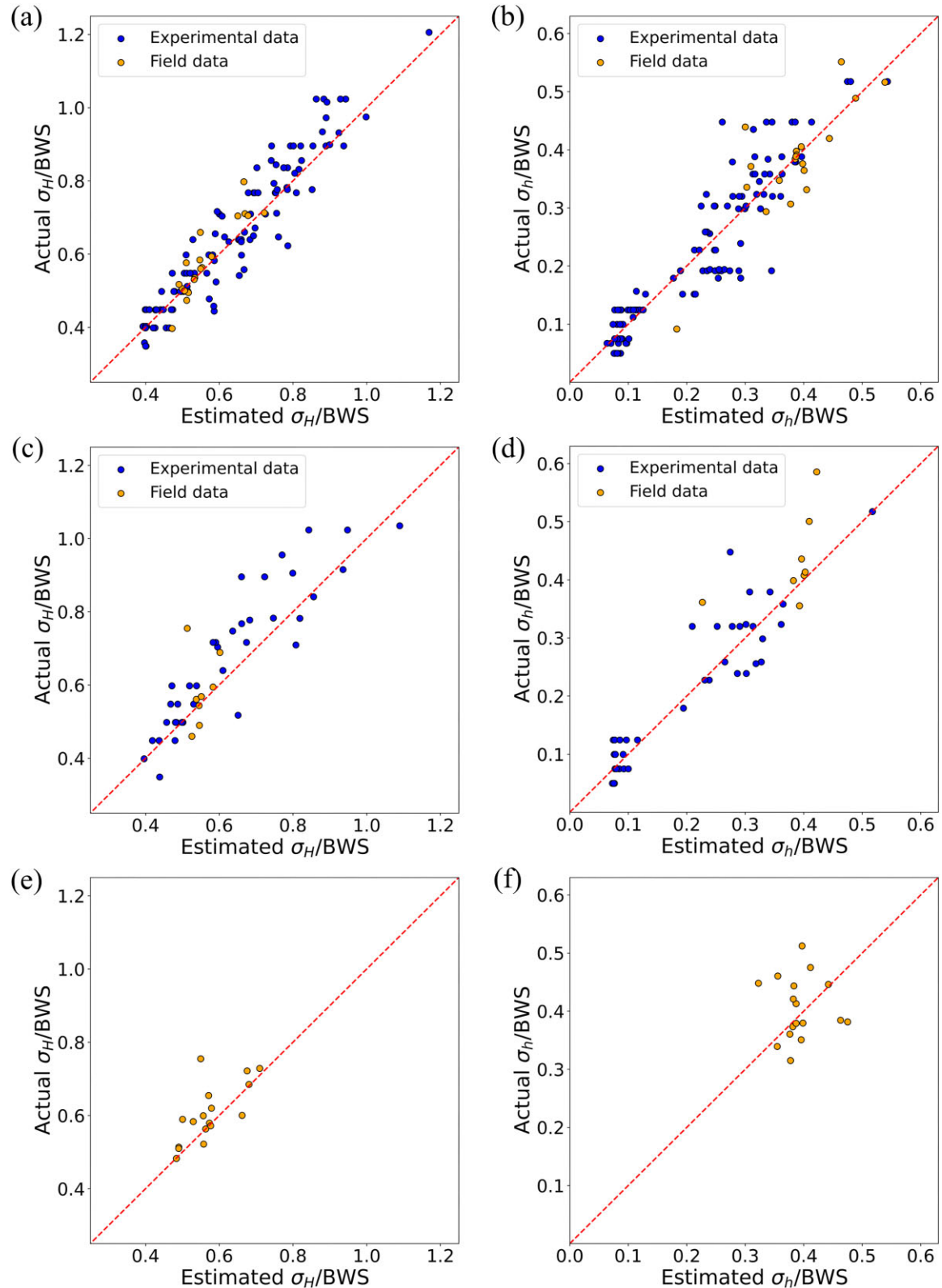
Figure 9. Comparison of estimated and actual σ_H/BWS and σ_h/BWS values. Training data set: (a) σ_H/BWS; (b) σ_h/BWS. Testing data set: (c) σ_H/BWS; (d) σ_h/BWS. Validation data set: (e) σ_H/BWS; (f) σ_h/BWS.

over the 79 experimental data points used in Lin's model. The quality of the experimental data is also enhanced, as they are obtained using the PS approach, whereas the experimental data set in Lin's study contains a mixture of PD and PS data. Secondly, considering θ_b and *L/R* share different formation mechanisms (Lee

et al., 2016; Xiang *et al.*, 2024b), the proposed model utilizes both breakout geometries as input parameters, whereas only θ_b is employed by Lin's model. Moreover, in this study, the principal stresses are normalized by BWS values to address the discrepancies between the experimental and field data, which is expected to further enhance

Table 1. Estimation accuracies of σ_H and σ_h.

		Number of data	MAPE (per cent)	RMSE (MPa)
Model development data set	σ_H (Training)	131	7.12	8.96
	σ_H (Testing)	46	10.37	14.55
	σ_H (Overall)	177	7.96	10.70
	σ_h (Training)	131	19.78	6.60
	σ_h (Testing)	46	19.15	7.73
	σ_h (Overall)	177	19.62	6.91
Model validation data set	σ_H	17	6.79	2.14
	σ_h	17	12.49	1.86
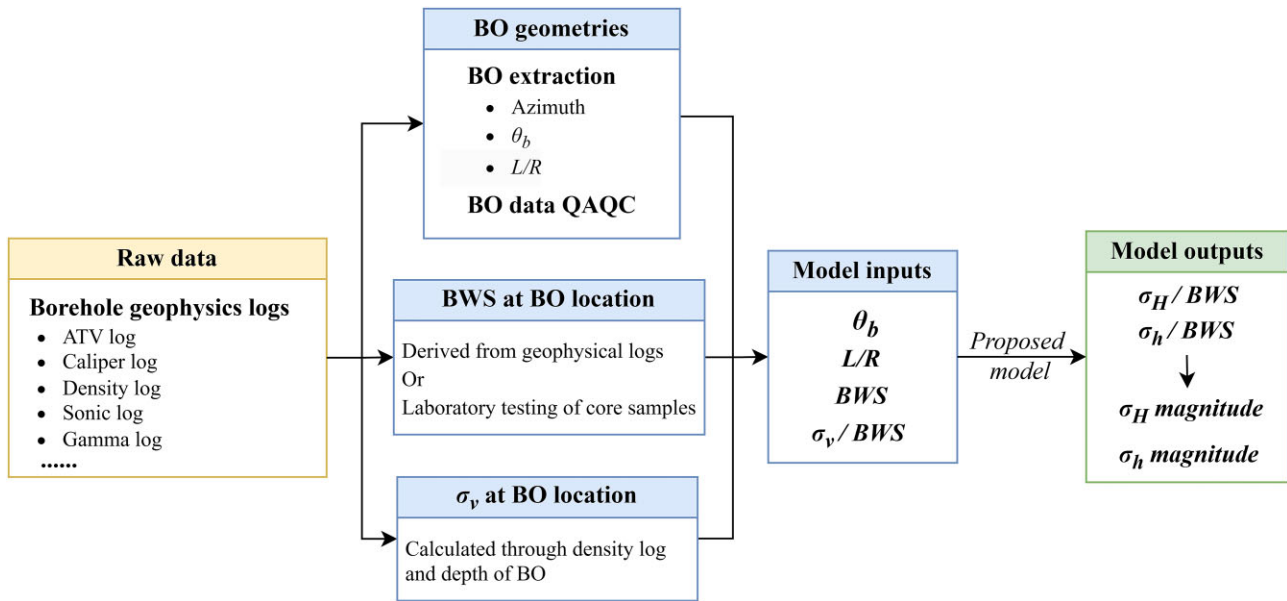
Figure 10. Schematic flowchart of the model application procedure.

the accuracy and generalizability of the proposed model compared to Lin's model.

4 MODEL APPLICATION AND FURTHER VALIDATION

The flowchart for the application of the proposed model is shown in Fig. 10. The input parameters can be primarily obtained from borehole geophysical logs, and the outputs are the magnitudes of the two principal horizontal stresses. The effectiveness of the model is further demonstrated and verified in this section by applying it to additional BOs collected from Mine A and another longwall coal mine in Australia (Mine B). These data are independent of the 177 data points used in model development, ensuring an unbiased evaluation of the model's generalizability.

4.1. Model application and further validation in Mine A

Apart from the 34 BOs collected in Section 2.2 and utilized for the model development, additional BO data points are extracted from a group of five adjacent exploration boreholes (BH-A1 to BH-A5) in Mine A. The same BO extraction and QAQC procedures introduced in Section 2.2 are applied to the data obtained from these boreholes. A total of 63 BOs are obtained, and their distributions are

shown in Fig. 11(a). *In-situ* stress measurements were conducted in these boreholes between 350 and 530 m using the overcoring method.

As indicated in Fig. 11(b), the averaged azimuth of the 63 BOs is around 128°/308° ± 12°, which is closely aligned with the measured σ_h directions. The estimated stress magnitudes by the proposed model are plotted against the stress measurements in Figs 11(c) (σ_H) and (d) (σ_h). To account for model uncertainties, error bars are incorporated into the predictions based on the MAPE of the model development data set (±7.96 per cent for σ_H and ±19.62 per cent for σ_h). Compared to the point overcoring stress measurements at depths of 350 to 530 m, the large quantity of BO data allows for a more continuous and detailed stress profile to be established over a greater depth range (240 to 570 m). The estimated stresses are in good agreement with the measured values and effectively capture the overall trend of stress variations with depth. Furthermore, clusters of BOs are observed at depths of 230–270, 295 and 400 m, showing relatively consistent stress estimations, with σ_H concentrated at approximately 10 ± 2, 11.5 ± 2 and 15 ± 2.5 MPa, respectively, and σ_h at 8.50 ± 1.5, 8.5 ± 1 and 11.5 ± 2 MPa, respectively. These clusters indicate that the local stress environments at these depths are relatively uniform, with low spatial variability in stress magnitudes across the boreholes. On the other hand, the estimated stresses at depths of
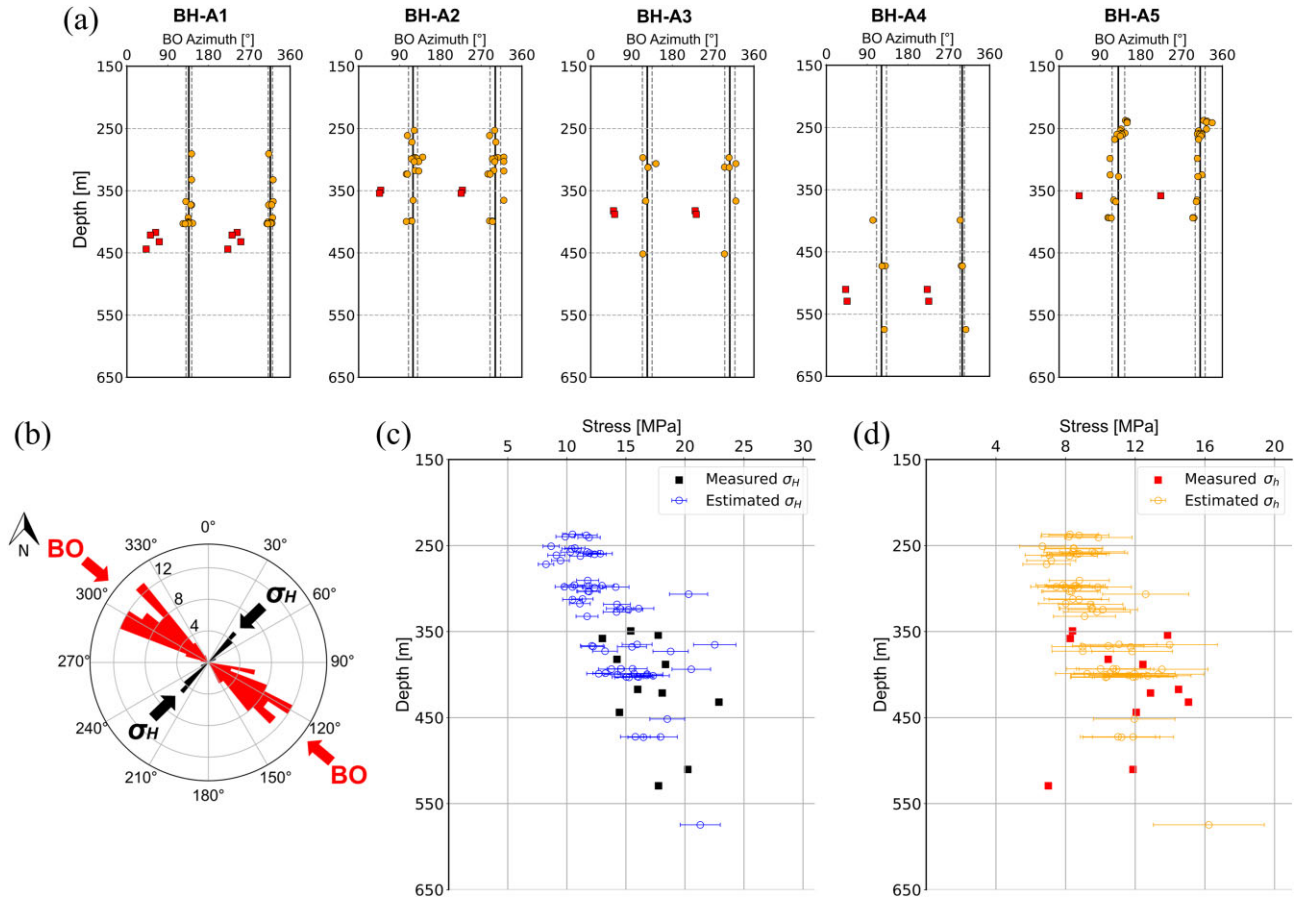
Figure 11. Model application in BH-A1 to BH-A5. (a) Distributions of obtained BOs (orange points) and stress measurements (red points); (b) Orientations of BOs relative to the measured σ_H direction. The radial axis represents the number of data; (c) Measured (black points) and estimated σ_H (blue points and error bars) magnitudes with depth; (d) Measured (red points) and estimated σ_h (orange points and error bars) magnitudes with depth.

370 m are relatively scattered, suggesting relatively higher stress variability at this depth. Additionally, a notably high σ_H point over 20 MPa is identified at 306 m, which may represent a potential high-stress zone.

4.2. Model application in Mine B

Mine B is located in the western part of the Sydney Basin region, which is situated in a different stress province than that of Mine A, as illustrated in Fig. 3. Borehole geophysical logs from 11 boreholes (BH-B1 to BH-11) are analysed, and a total of 103 BOs at depths between 240 and 450 m are extracted following the procedures described in Section 2.2. These boreholes are divided into three subsets based on their spatial locations. The first subset contains six boreholes (BH-B1 to BH-B6), as illustrated in Fig. 12(a). The average σ_H direction in these boreholes derived from BO azimuths is around 54°/232° (NE-SW), with a standard deviation of approximately 16°–19°. The second (Fig. 12d) and third (Fig. 12g) subsets comprise two (BH-B7 to BH-B8) and three boreholes (BH-B9 to BH-B11), respectively. In comparison to the first set of boreholes, the σ_H directions in the second and third sets of boreholes exhibit a clockwise rotation, orienting at around 90°/180° (E-W), with standard deviations ranging from 10° to 16°. The stress estimation results for the three sets of data are exhibited in Figs 12(c), 12(f)

and 12(i). Continuous and detailed stress profiles, similar to those shown in Fig. 11, are established in all three sets of boreholes. The estimated σ_H magnitudes primarily range from 15 to 30 MPa, while the estimated σ_h varies between 10 and 20 MPa. The local stress fields in the vicinity of these boreholes are estimated to be under the TF stress regimes. Although no stress measurement data are available for direct comparison, the estimated stress orientations and magnitudes closely align with the mine site operational experiences in the region and historical stress measurements in the Western Sydney Basin (Hillis *et al*., 1999; Burra *et al*., 2014; Rajabi *et al*., 2017). Furthermore, the estimated stresses in these boreholes exhibit considerably more variability in comparison to that of Mine A (Figs 11c and 11d), with stress rotations between boreholes and horizontal to vertical stress ratios of up to 3:1, which is also consistent with the previous observations reported for the Sydney Basin (Hebblewhite & Lu, 2004; Rajabi et al., 2016, 2017).

The above analysis based on 166 BO data points from 16 boreholes across two mine sites has demonstrated the proposed model's effectiveness in estimating both horizontal stresses. The abundance of BO data enables the model to characterize local stress fields with greater detail compared to conventional stress measurement techniques. Moreover, depending on the design and location of the underground operations, the model can either reduce the need for
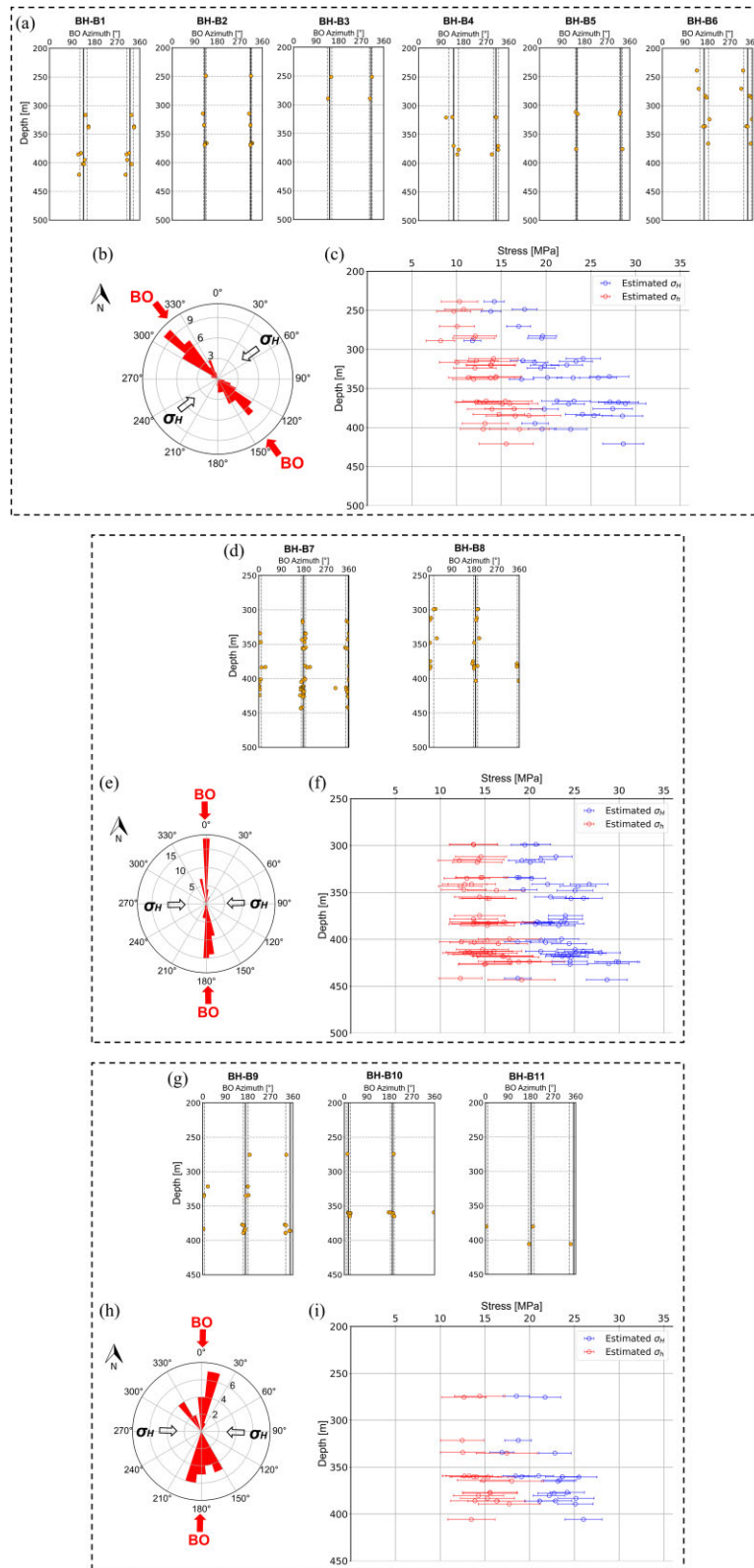
Figure 12. Model application in Mine B. Distribution of selected BOs for the three sets of boreholes are shown in (a), (d) and (g); Orientations of BOs and estimated σ_H directions are presented in (b), (e) and (h). The radial axis represents the number of data; Estimated σ_H and σ_h magnitudes are exhibited in (c), (f) and (i).

further *in-situ* stress measurements or provide valuable guidance on selecting additional stress testing locations.

5 DISCUSSION

As indicated in Fig. 9 and Table 1, the model tends to yield more accurate σ_H estimations compared to σ_h. This discrepancy is believed to be primarily attributed to the varied sensitivities of the BO extent to σ_H and σ_h. Along the σ_h direction around the borehole, the magnitude of the redistributed major principal stress is predominantly affected by σ_H. As a result, experimental and numerical observations have well established that σ_H has considerably greater impacts on both θ_b and *L/R* in comparison to σ_h (Haimson & Lee, 2004; Lee *et al*., 2016; Xiang *et al*., 2023a). This is also evident from the correlation coefficients shown in Fig. 7. More specifically, analysis of 29 PS experiments in Gosford sandstone reveals that variations of 10 MPa in σ_H correspond to average changes ranging from 9° to 15° and 0.16 to 0.24 in θ_b and *L/R*, respectively, whereas a 10 MPa change in σ_h magnitude yields average variations of 1.5° to 6° in θ_b and 0.06 to 0.09 in *L/R* (Xiang *et al*., 2024b). Nevertheless, given that the σ_H magnitude is generally considered more critical in practical applications compared to σ_h, the relatively high errors associated with σ_h are deemed acceptable.

The model errors and uncertainties can be predominantly explained by two factors. First, due to the design of the experiments, only one stress was altered between most experiments for quantitative analysis. Consequently, multiple BO geometries and σ_v/BWS values may be associated with the same σ_H/BWS or σ_h/BWS (Fig. 7). This leads to multiple estimated values corresponding to one actual experimental data point (Figs 9a–d) and introduces uncertainties in the estimation of both experimental and field data. Secondly, as exhibited in Fig. 6, the experimental data set contains notably different stress ranges than the field data set. Despite scaling the stress values by BWS, some σ_h/BWS values of the field data can extend beyond the range of the experimental data set (Fig. 7). As the model training primarily relies on experimental data, this out-of-range issue can result in relatively high estimation discrepancies for σ_h/BWS in the field data, further contributing to the accuracy difference between estimated σ_H and σ_h. To reduce the model uncertainties and further improve its accuracy, it is suggested to incorporate additional data that cover a broader range of stress conditions with more systematic variations.

In contrast to prior models, this study adopts a different approach by scaling all three principal stresses by BWS to address the stress magnitude discrepancies between experimental and field data. Additionally, BWS values are incorporated as input parameters, assigning a dual significance to BWS in the model. Consequently, BWS becomes pivotal for model performance. Since retrieving core samples at the BO locations and conducting laboratory tests are difficult and impractical in most field conditions, further investigation into the correlation between borehole geophysical logs and rock strength, along with the continued development of models such as those proposed in Chang *et al*. (2006) and Xiang *et al*. (2023c), is critical for obtaining accurate stress estimations from BO data.

While the proposed model has demonstrated robust performance in estimating both horizontal stress magnitudes across two mine sites, it is important to acknowledge the potential for further development. Given the difficulties and high expenses of conducting PS experiments, borehole logging and *in-situ* stress measurements, obtaining BO data for model development is challenging. The current data set is composed of 194 data points, significantly exceeding the amount used in previous studies. Nonetheless, the model's applicability could still be enhanced by including more data with various rock types and stress regimes, especially data on igneous and metamorphic rocks, as the current data set is predominantly composed of sedimentary rocks. Furthermore, numerical simulations (Sahara *et al*., 2017; Xiang *et al*., 2023b) and generative artificial intelligence models such as Generative Adversarial Networks (GAN) (Wu *et al*., 2024) can be also applied to provide supplementary data for model development. Nevertheless, the validity of these artificially generated data needs to be carefully examined and further evaluated. Additionally, the model can be further developed by incorporating the impacts of geological structures and thermal effects, broadening its capability to characterize stress distribution around major geological structures and under deep geothermal conditions (Andersson *et al*., 2009; Duan & Kwok, 2016; Trzeciak *et al*., 2021; S. Zhang *et al*., 2023).

6 CONCLUSIONS

This study presents a new BPNN model to estimate both horizontal stress magnitudes from multiscale borehole BO data. For this purpose, borehole geophysical logs and *in-situ* stress measurements are obtained from a mine site in the Bowen Basin, Australia and a data set of 150 PS experimental data and 44 field-scale data points is compiled for model development and validation. To address the stress magnitude discrepancies between experimental and field data, the three principal stresses are normalized by rock BWS. Consequently, the model utilizes θ_b, *L/R*, BWS and σ_v/BWS as input parameters, with σ_H/BWS and σ_h/BWS as target outputs.

In the model development data set, the model achieves MAPEs and RMSEs of 7.96 per cent and 10.35 MPa for σ_H and 19.62 per cent and 6.92 MPa for σ_h, respectively. The accuracies are slightly improved in the validation data set, with MAPE at 6.8 per cent (σ_H) and 12.49 per cent (σ_h) and RMSE at 2.14 MPa (σ_H) and 1.86 MPa (σ_h). The discrepancies between σ_H and σ_h accuracies are attributed to their different impacts on BO geometries, with BO formation being generally more sensitive to the variation of σ_H. Additionally, 166 BO data points, independent of those employed for model development, are collected from 16 boreholes in two mine sites to examine the model's effectiveness and generalizability. Continuous and detailed stress profiles are established through these BO data, which are in good agreement with either the stress measurements in these boreholes or historical stress data in the region.

The proposed model offers an accurate and cost-effective approach for *in-situ* stress estimation, as its input parameters can be primarily derived from borehole geophysical logs. The model's generalizability and reliability are significantly improved over previous studies by scaling stress values based on BWS and being developed on a data set with enhanced data quantity and quality. Moving forward, further development can be made to the model by expanding the data set to include more diverse rock types and considering the impacts of geological structures and temperature variations on BO formation.

DATA AVAILABILITY

The borehole BO data set used for model development is listed in Appendix A.

REFERENCES

Amadei, B. & Stephansson, O., 1997. *Rock Stress and Its Measurement*(1st ed.). Chapman & Hall.

Anderson, E.M., 1905. The dynamics of faulting, *Trans. Edinb. Geol. Soc.* **8,** 387–402.

Andersson, J.C., Martin, C.D. & Stille, H., 2009. The Äspö Pillar Stability Experiment: Part II—Rock mass response to coupled excavation-induced and thermal-induced stresses, *Int. J. Rock Mech. Min. Sci.* **46,** 879–895.

Barton, C.A., Zoback, M.D. & Burns, K.L., 1988. In-situ stress orientation and magnitude at the Fenton Geothermal Site, New Mexico, determined from wellbore breakouts, *Geophys. Res. Lett.* **15,** 467–470.

Bažant, Z.P., Lin, F.-B. & Lippmann, H., 1993. Fracture energy release and size effect in borehole breakout, *Int. J. Numer. Anal. Methods Geomech.* **17,** 1–14.

Bergen, K.J., Johnson, P.A., de Hoop, M.V. & Beroza, G.C., 2019. Machine learning for data-driven discovery in solid Earth geoscience, *Science* **363,** eaau0323, doi:10.1126/science.aau0323.

Bergstra, J., Bardenet, R., Bengio, Y. & Kégl, B., 2011. Algorithms for hyper-parameter optimization, *Proc. Adv. Neural Inform. Process. Syst.,* **24,** 2546–2554.

Borm, G., Engeser, B., Hoffers, B., Kutter, H.K. & Lempp, C., 1997. Borehole instabilities in the KTB main borehole, *J. geophys. Res. Solid Earth* **102,** 18 507–18 517.

Burra, A., Esterle, J.S. & Golding, S.D., 2014. Horizontal stress anisotropy and effective stress as regulator of coal seam gas zonation in the Sydney Basin, Australia, *Int. J. Coal Geol.* **132,** 103–116.

Ceryan, N., Ozkat, E.C., Korkmaz Can, N. & Ceryan, S., 2021. Machine learning models to estimate the elastic modulus of weathered magmatic rocks, *Environ. Earth Sci.* **80,** 448, doi:10.1007/s12665-021-09738-9.

Chang, C., Zoback, M.D. & Khaksar, A., 2006. Empirical relations between rock strength and physical properties in sedimentary rocks, *J. Pet. Sci. Eng.* **51,** 223–237.

Cox, J.W., 1972. The high-resolution dipmeter reveals dip-related borehole and formation characteristics, *J. Can. Pet. Technol.* **11,** doi:10.2118/72-01-02.

Dresen, G., Stanchits, S. & Rybacki, E., 2010. Borehole breakout evolution through acoustic emission location analysis, *Int. J. Rock Mech. Min. Sci.* **47,** 426–435.

Duan, K. & Kwok, C.Y., 2016. Evolution of stress-induced borehole breakout in inherently anisotropic rock: insights from discrete element modeling, *J. geophys. Res. Solid Earth* **121,** 2361–2381.

Eberhardt, E., 2001. Numerical modelling of three-dimension stress rotation ahead of an advancing tunnel face, *Int. J. Rock Mech. Min. Sci.* **38,** 499–518.

Fairhurst, C., 2003. Stress estimation in rock: a brief history and review, *Int. J. Rock Mech. Min. Sci.,* Special Issue of the IJRMMS: Rock Stress Estimation ISRM Suggested Methods and Associated Supporting Papers, **40,** 957–973.

Figueiredo, B., Lamas, L. & Muralha, J., 2010. Determination of In situ stresses using large flat jack tests. *Paper presented at the ISRM International Symposium - 6th Asian Rock Mechanics Symposium,* New Delhi, India.

Furtney, J.K., Thielsen, C., Fu, W. & Le Goc, R., 2022. Surrogate models in rock and soil mechanics: integrating numerical modeling and machine learning, *Rock Mech. Rock Eng.* **55,** 2845–2859.

Garavand, A. & Hadavimoghaddam, F., 2023. In situ stress assessment based on plastic behavior of borehole breakouts and machine learning, *Int. J. Numer. Anal. Methods Geomech.* **47,** 241–260.

Gough, D.I. & Bell, J.S., 1981. Stress orientations from oil-well fractures in Alberta and Texas, *Can. J. Earth Sci.* **18,** 638–645.

Haimson, B., 2007. Micromechanisms of borehole instability leading to breakouts in rocks, *Int. J. Rock Mech. Min. Sci.* **44,** 157–173.

Haimson, B. & Kovacich, J., 2003. Borehole instability in high-porosity Berea sandstone and factors affecting dimensions and shape of fracture-like breakouts, *Eng. Geol.* **69,** 219–231.

Haimson, B. & Lee, H., 2004. Borehole breakouts and compaction bands in two high-porosity sandstones, *Int. J. Rock Mech. Min. Sci.* **41,** 287–301.

Haimson, B.C. & Cornet, F.H., 2003. ISRM suggested methods for rock stress estimation—Part 3: hydraulic fracturing (HF) and/or hydraulic testing of pre-existing fractures (HTPF), *Int. J. Rock Mech. Min. Sci.,* Special Issue of the IJRMMS: Rock Stress Estimation ISRM Suggested Methods and Associated Supporting Papers **40,** 1011–1020.

Hebblewhite, B.K. & Lu, T., 2004. Geomechanical behaviour of laminated, weak coal mine roof strata and the implications for a ground reinforcement strategy, *Int. J. Rock Mech. Min. Sci.* **41,** 147–157.

Heidbach, O., *et al.* 2018. The World Stress Map database release 2016: crustal stress pattern across scales, *Tectonophysics* **744,** 484–498.

Herrick, C.G. & Haimson, B.C., 1994. Modeling of episodic failure leading to borehole breakouts in Alabama limestone, *Presented at the 1st North American Rock Mechanics Symposium,* Austin, Texas, ARMA–1994-0217.

Hillis, R.R., Enever, J.R. & Reynolds, S.D., 1999. In situ stress field of eastern Australia, *Aust. J. Earth Sci.* **46,** 813–825.

Jo, Y., Chang, C., Ji, S.-H. & Park, K.-W., 2019. In situ stress states at KURT, an underground research laboratory in South Korea for the study of high-level radioactive waste disposal, *Eng. Geol.* **259,** 105198, doi:10.1016/j.enggeo.2019.105198.

Kim, H., Xie, L., Min, K.-B., Bae, S. & Stephansson, O., 2017. Integrated In situ stress estimation by hydraulic fracturing, borehole observations and numerical analysis at the EXP-1 borehole in Pohang, Korea, *Rock Mech. Rock Eng.* **50,** 3141–3155.

Lai, C.Y., Wong, L.N.Y. & Wallace, M., 2019. Review and assessment of In-situ rock stress in Hong Kong for territory-wide geological domains and depth profiling, *Eng. Geol.* **248,** 267–282.

Lavrov, A., 2003. The Kaiser effect in rocks: principles and stress estimation techniques, *Int. J. Rock Mech. Min. Sci.* **40,** 151–171.

Lee, H., Moon, T. & Haimson, B.C., 2016. Borehole breakouts induced in arkosic sandstones and a discrete element analysis, *Rock Mech. Rock Eng.* **49,** 1369–1388.

LeRiche, A.C., 2017. *Stress Estimation from Borehole Scans for Prediction of Excavation Overbreak in Brittle Rock (M.A.Sc.).* Queen's University

Li, Y., Rahardjo, H., Satyanaga, A., Rangarajan, S. & Lee, D.T.-T., 2022. Soil database development with the application of machine learning methods in soil properties prediction, *Eng. Geol.* **306,** 106769, doi:10.1016/j.enggeo.2022.106769.

Lin, H., Kang, W.-H., Oh, J. & Canbulat, I., 2020a. Estimation of in-situ maximum horizontal principal stress magnitudes from borehole breakout data using machine learning, *Int. J. Rock Mech. Min. Sci.* **126,** 104199, doi:10.1016/j.ijrmms.2019.104199.

Lin, H., Oh, J., Canbulat, I., Hebblewhite, B., Masoumi, H. & Walsh, S., 2021. Experimental study on borehole size effect and prediction of breakout initiation stress, *Int. J. Rock Mech. Min. Sci.* **142,** 104762, doi:10.1016/j.ijrmms.2021.104762.

Lin, H., Oh, J., Canbulat, I. & Stacey, T.R., 2020b. Experimental and analytical investigations of the effect of hole size on borehole breakout geometries for estimation of In situ stresses, *Rock Mech. Rock Eng.* **53,** 781–798.

Lin, H., Singh Kumar, S., Xiang, Z., Hee Kang, W., Raval, S., Oh, J. & Canbulat, I., 2022. An investigation of machine learning techniques to

estimate minimum horizontal stress magnitude from borehole breakout, *Int. J. Min. Sci. Technol.* **32,** 1021–1029.

Lin, H., Singh, S., Oh, J., Canbulat, I., Kang, W.H., Hebblewhite, B. & Stacey, T.R., 2020c. A combined approach for estimating horizontal principal stress magnitudes from borehole breakout data via artificial neural network and rock failure criterion, *Int. J. Rock Mech. Min. Sci.* **136,** 104539, doi:10.1016/j.ijrmms.2020.104539.

Ljunggren, C., Chang, Y., Janson, T. & Christiansson, R., 2003. An overview of rock stress measurement methods, *Int. J. Rock Mech. Min. Sci.,* Special Issue of the IJRMMS: Rock Stress Estimation ISRM Suggested Methods and Associated Supporting Papers **40,** 975–989.

Lucier, A.M., Zoback, M.D., Heesakkers, V., Reches, Z. & Murphy, S.K., 2009. Constraining the far-field in situ stress state near a deep South African gold mine, *Int. J. Rock Mech. Min. Sci.* **46,** 555–567.

Mahmoodzadeh, A., Mohammadi, M., Ghafoor Salim, S., Farid Hama Ali, H., Hashim Ibrahim, H., Nariman Abdulhamid, S., Nejati, H.R. & Rashidi, S., 2022. Machine learning techniques to predict rock strength parameters, *Rock Mech. Rock Eng.* **55,** 1721–1741.

Martin, C.D., 1997. Seventeenth Canadian Geotechnical colloquium: the effect of cohesion loss and stress path on brittle rock strength, *Can. Geotech. J.* **34,** 698–725.

Martin, C.D., Martino, J.B. & Dzik, E.J., 1994. Comparison of borehole breakouts from laboratory and field tests. In: *Proceedings Eurock'94, SPE/ISRM Rock Mechanics in Petroleum Engineering Conference,* Delft, A.A. Balkema, Rotterdam, pp. 183–190.

Papamichos, E., 2010. Borehole failure analysis in a sandstone under anisotropic stresses, *Int. J. Numer. Anal. Methods Geomech.* **34,** 581–603.

Pierdominici, S., *et al.* 2020. Stress field interactions between overlapping shield volcanoes: borehole breakout evidence from the Island of Hawai'i, USA, *J. geophys. Res. Solid Earth* **125,** e2020JB019768, doi:10.1029/2020JB019768.

Qian, W. & Pedersen, L.B., 1991. Inversion of borehole breakout orientation data, *J. geophys. Res. Solid Earth* **96,** 20093–20107.

Qiao, Y., Cheng, T., He, M., Li, H., Xiao, Y. & Tang, J., 2024. Water content effect on borehole breakout in hard rock and its interpretation: an experimental study, *Rock Mech. Rock Eng.* **57,** 6715–6737.

Rajabi, M., Tingay, M. & Heidbach, O., 2016. The present-day stress field of New South Wales, Australia, *Aust. J. Earth Sci.* **63,** 1–21.

Rajabi, M., Tingay, M., Heidbach, O., Hillis, R. & Reynolds, S., 2017. The present-day stress field of Australia, *Earth-Sci. Rev.* **168,** 165–189.

Sahara, D.P., Schoenball, M., Gerolymatou, E. & Kohl, T., 2017. Analysis of borehole breakout development using continuum damage mechanics, *Int. J. Rock Mech. Min. Sci.* **97,** 134–143.

Shen, B., 2008. Borehole breakouts and In situ stresses, in Potvin, Y, Carter, J, Dyskin, A & Jeffrey, R(eds), *SHIRMS 2008: Proceedings of the First Southern Hemisphere International Rock Mechanics Symposium, Australian Centre for Geomechanics,* Perth, 407–418.

Sjöberg, J., Christiansson, R. & Hudson, J.A., 2003. ISRM suggested methods for rock stress estimation—Part 2: overcoring methods, *Int. J. Rock Mech. Min. Sci.,* Special Issue of the IJRMMS: Rock Stress Estimation ISRM Suggested Methods and Associated Supporting Papers **40,** 999–1010.

Sjöberg, J. & Klasson, H., 2003. Stress measurements in deep boreholes using the *Borre* (SSPB) probe, *Int. J. Rock Mech. Min. Sci.,* Special Issue of the IJRMMS: Rock Stress Estimation ISRM Suggested Methods and Associated Supporting Papers **40,** 1205–1223.

Snee, J.-E.L. & Zoback, M.D., 2018. State of stress in the Permian Basin, *Texas and New Mexico: Implications for induced seismicity. Lead. Edge* **37,** 127–134.

Song, I., 1998. Borehole Breakouts and Core Disking in Westerly Granite: Mechanisms of Formation and Relationship to in Situ Stress, *PhD thesis.* University of Wisconsin, Madison, Wisconsin.

Trzeciak, M., Sone, H., Voegeli, S., Bate, C.E. & Wang, H., 2021. Laboratory evaluation of the thermal breakout method for maximum horizontal stress measurement, *Rock Mech. Rock Eng.* **55,** 51–69,

Vernik, L. & Zoback, M.D., 1992. Estimation of maximum horizontal principal stress magnitude from stress-induced well bore breakouts in the Cajon Pass Scientific Research borehole, *J. geophys. Res. Solid Earth* **97,** 5109–5119.

Walton, G., Kalenchuk, K.S., Hume, C.D. & Diederichs, M.S., 2015. Borehole breakout analysis to determine the In-situ stress State in hard rock. *49th U.S. Rock Mechanics/Geomechanics Symposium,* ARMA–2015-553, San Francisco, California.

Wang, W. & Schmitt, D.R., 2020. Automated borehole breakout interpretation from ultrasonic imaging: application to a deep borehole drilled into the crystalline crust. *Presented at the 54th U.S. Rock Mechanics/Geomechanics Symposium,* ARMA–2020-1270.

Wang, W., Schmitt, D.R. & Chan, J., 2023. Heterogeneity versus anisotropy and the State of stress in stable cratons: observations from a deep borehole in northeastern Alberta, Canada, *J. geophys. Res. Solid Earth* **128,** e2022JB025287, doi:10.1029/2022JB025287.

Wu, B., Zhang, H., Wu, S., Nie, Y., Zhang, X. & Jeffrey, R.G., 2024. Prediction of the maximum horizontal principal stress from breakout data using generative adversarial networks and backpropagation neural network, *SPE J.* **29,** 606–619.

Xiang, Z., Moon, T., Oh, J., Li, X., Si, G. & Canbulat, I., 2023a. Numerical investigation of borehole breakout and rock spalling based on strain energy criteria, *Int. J. Rock Mech. Min. Sci.* **171,** 105587, doi:10.1016/j.ijrmms.2023.105587.

Xiang, Z., Moon, T., Oh, J., Si, G. & Canbulat, I., 2024a. Analytical investigations of in situ stress inversion from borehole breakout geometries, *J. Rock Mech. Geotech. Eng.* **16,** 2375–2387.

Xiang, Z., Moon, T., Si, G., Oh, J. & Canbulat, I., 2023b. Numerical analysis of V-shaped borehole breakout using three-dimensional discrete-element method, *Rock Mech. Rock Eng.* **56,** 3197–3214.

Xiang, Z., Oh, J., Si, G. & Canbulat, I., 2024b. Parametric analysis of borehole breakout and spalling phenomena: an experimental investigation, *Rock Mech. Rock Eng.* **57,** 11207–11222,

Xiang, Z., Si, G., Oh, J., Canbulat, I. & Li, C.C., 2024c. Experimental investigation of borehole breakout formation in Gosford sandstone, *Int. J. Rock Mech. Min. Sci.* **180,** 105824, 10.1016/j.ijrmms.2024.105824.

Xiang, Z., Yu, Z., Kang, W.-H., Si, G., Oh, J. & Canbulat, I., 2023c. Estimation of *in-situ* rock strength from borehole geophysical logs in Australian coal mine sites, *Int. J. Coal Geol.* **269,** 104210, doi:10.1016/j.coal.2023.104210.

Zhang, H. & Yin, S., 2019. Inference of *in situ* stress from thermoporoelastic borehole breakouts based on artificial neural network, *Int. J. Numer. Anal. Methods Geomech.* **43,** 2493–2511.

Zhang, H., Yin, S. & Aadnoy, B.S., 2018. Poroelastic modeling of borehole breakouts for *in-situ* stress determination by finite element method, *J. Pet. Sci. Eng.* **162,** 674–684.

Zhang, S., Ma, X., Bröker, K., van Limborgh, R., Wenning, Q., Hertrich, M. & Giardini, D., 2023. Fault zone spatial stress variations in a granitic rock mass: revealed by breakouts within an array of boreholes, *J. geophys. Res. Solid Earth* **128,** e2023JB026477, doi:10.1029/2023JB026477.

Zhang, W., Gu, X., Hong, L., Han, L. & Wang, L., 2023. Comprehensive review of machine learning in geotechnical reliability analysis: algorithms, applications and further challenges, *Appl. Soft Comput.* **136,** 110066, doi:10.1016/j.asoc.2023.110066.

Zhang, YZ., Dusseault, M.B. & Yassir, N.A., 1994. Effects of rock anisotropy and heterogeneity on stress distributions at selected sites in North America, *Eng. Geol.* **37,** 181–197.

Zoback, M.D., *et al.* 2003. Determination of stress orientation and magnitude in deep wells, *Spec. Issue IJRMMS Rock Stress Estim. ISRM Suggest. Methods Assoc. Support. Pap.* **40,** 1049–1076.

Zoback, M.D., Moos, D., Mastin, L. & Anderson, R.N., 1985. Well bore breakouts and *in situ* stress, *J. geophys. Res. Solid Earth* **90,** 5523–5530.

Appendix A: Supplementary data

Table A1. PS experimental BO data used for model development.

	σ_H (MPa)	σ_h (MPa)	σ_v (MPa)	θ_b (°)	L/R	BWS (MPa)
Alabama limestone (Herrick & Haimson, 1994)	41	14	21	45	1.18	92.33
	50	14	21	55	1.32	92.33
	57.5	14	21	65.5	1.56	92.33
	65.5	14	21	81.5	1.76	92.33
	51.5	21	28	53.5	1.2	92.33
	58.5	21	28	56	1.27	92.33
	65.5	21	28	63	1.46	92.33
	65.5	21	28	65.5	1.56	92.33
	72.2	21	28	70	1.64	92.33
	75.8	21	28	80	1.98	92.33
	58.5	28	35	52	1.22	92.33
	65.5	28	35	55.5	1.24	92.33
	72.2	28	35	68	1.6	92.33
	79	28	35	70	1.7	92.33
	83	28	35	86	2	92.33
	62	35	42	45	1.13	92.33
	69	35	42	57	1.27	92.33
	79	35	42	64	1.6	92.33
	84.5	35	42	86	1.94	92.33
	90	35	42	88	2.08	92.33
Tablerock sandstone (Haimson & Lee, 2004)	40	15	30	35	1.11	83.74
	50	15	30	51.5	1.22	83.74
	60	15	30	65	1.43	83.74
	70	15	30	73	1.558	83.74
	60	20	40	63	1.3	83.74
	70	20	40	67.5	1.618	83.74
	80	20	40	73	1.875	83.74
	60	25	40	64	1.175	83.74
	70	25	40	71	1.74	83.74
	75	25	40	75	1.68	83.74
	85	25	40	82	1.835	83.74
	54.9	30	40	53	1.15	83.74
	60	30	40	64	1.16	83.74
	65.1	30	40	79.5	1.3	83.74
Tenino sandstone (Lee *et al.*, 2016)	35.4	15	25	45	1.2	77.30
	50.25	15	25	59	1.77	77.30
	65.25	15	25	63.5	1.82	77.30
	40	20	30	48	1.15	77.30
	50	20	30	68	1.52	77.30
	60	20	30	73.5	1.625	77.30
	70	20	30	78.5	1.92	77.30
	45	25	35	61.5	1.19	77.30
	50	25	35	66	1.41	77.30
	55	25	35	70	2.23	77.30
	60.5	25	35	72	2.07	77.30
	65	25	35	77	2.33	77.30
	40.5	30	40	56	1.12	77.30
	51	30	40	70.3	1.46	77.30
	60	30	40	77.5	2.02	77.30
	60	40	50	68	1.28	77.30
	72	40	50	73.6	2.13	77.30
	80	40	50	82	2.36	77.30
	93.2	40	50	85	2.53	77.30

Table A1. Continued

	σ_H (MPa)	σ_h (MPa)	σ_v (MPa)	θ_b (°)	L/R	BWS (MPa)
Westerly granite (Song, 1998)	140	20	20	34.58	1.142	401.53
	140	20	40	39.77	1.22	401.53
	140	20	60	28.32	1.125	401.53
	160	20	20	43.18	1.276	401.53
	160	20	40	42.44	1.26	401.53
	160	20	60	32.12	1.168	401.53
	180	20	20	46.07	1.312	401.53
	180	20	40	42.62	1.268	401.53
	180	20	60	40.92	1.242	401.53
	200	20	20	45.86	1.318	401.53
	200	20	40	46.11	1.283	401.53
	200	20	60	44.82	1.287	401.53
	160	30	20	23.61	1.08	401.53
	160	30	40	14.3	1.033	401.53
	180	30	20	39.54	1.206	401.53
	180	30	40	32.61	1.209	401.53
	180	30	60	25.55	1.12	401.53
	200	30	20	38.16	1.261	401.53
	200	30	40	40.31	1.25	401.53
	200	30	60	36.8	1.249	401.53
	220	30	20	41.22	1.298	401.53
	220	30	40	41.22	1.274	401.53
	220	30	60	46.44	1.368	401.53
	240	30	20	36.8	1.308	401.53
	240	30	40	39.9	1.333	401.53
	240	30	60	40.7	1.331	401.53
	160	40	40	23.03	1.077	401.53
	160	40	60	24.38	1.09	401.53
	180	40	40	41.33	1.204	401.53
	180	40	60	30.88	1.139	401.53
	200	40	40	41.46	1.289	401.53
	200	40	60	39.68	1.28	401.53
	220	40	60	44.4	1.3	401.53
	220	40	40	52.87	1.347	401.53
	160	50	40	30.87	1.158	401.53
	160	50	60	25.42	1.124	401.53
	160	50	80	13.32	1.026	401.53
	180	50	40	39.28	1.218	401.53
	180	50	60	32.82	1.209	401.53
	180	50	80	25.07	1.274	401.53
	180	50	100	24.33	1.119	401.53
	180	50	120	15.85	1.057	401.53
	200	50	40	42.43	1.283	401.53
	200	50	60	42.24	1.271	401.53
	200	50	80	39.33	1.255	401.53
	200	50	100	37.57	1.243	401.53
	200	50	120	33.52	1.215	401.53
	220	50	40	45.13	1.294	401.53
	220	50	60	42.35	1.282	401.53
	220	50	80	40.96	1.256	401.53
	220	50	100	39.77	1.249	401.53
	220	50	120	39	1.238	401.53
	240	50	60	46.29	1.415	401.53
	240	50	80	47.47	1.306	401.53
	240	50	100	44.59	1.212	401.53

Table A1. Continued

	σ_H (MPa)	σ_h (MPa)	σ_v (MPa)	θ_b (°)	L/R	BWS (MPa)
Gosford sandstone (Xiang *et al.*, 2024b)	40	15	10	31	1.041	78.16
	50	15	10	59.5	1.259	78.16
	50	15	15	48	1.178	78.16
	50	20	15	48.5	1.159	78.16
	50	27	15	26	1.032	78.16
	50	15	20	45.5	1.116	78.16
	55	25	20	37	1.061	78.16
	60	15	10	60.5	1.376	78.16
	60	15	20	51	1.214	78.16
	60	15	30	41	1.148	78.16
	60	25	10	51.5	1.389	78.16
	60	25	20	48	1.126	78.16
	60	25	30	44	1.162	78.16
	60	35	20	45.5	1.083	78.16
	60	35	30	40	1.104	78.16
	70	15	20	64.5	1.498	78.16
	70	25	20	63.83	1.364	78.16
	70	35	20	58	1.231	78.16
	70	25	10	64.5	1.339	78.16
	70	25	30	60.5	1.300	78.16
	70	35	30	54	1.326	78.16
	70	35	35	47	1.160	78.16
	70	15	30	61	1.371	78.16
	80	15	20	73.5	1.753	78.16
	80	25	20	71.5	1.720	78.16
	80	35	20	67.5	1.603	78.16
	80	25	30	64.5	1.547	78.16
	80	25	36	61.5	1.540	78.16
	80	35	30	61.5	1.513	78.16
Gosford sandstone (This study)	50	20	20	37.3	1.046	78.16
	62	30	30	49.05	1.215	78.16
	55	28	21	37.6	1.043	78.16
	65	28	21	52.45	1.174	78.16
	73	28	21	60.47	1.352	78.16
	76	34	27	60.91	1.421	78.16
Yellow mudstone	80	15	10	43.5	1.164	223.52
	90	15	10	54	1.275	223.52
	90	15	20	45.5	1.121	223.52
	90	15	30	38.5	1.097	223.52
	90	25	20	36	1.061	223.52
	90	35	20	34	1.058	223.52
	100	15	10	62.5	1.296	223.52

Table A2. Field BO data used for model development and validation.

	σ_H (MPa)	σ_h (MPa)	σ_v (MPa)	θ_b (°)	L/R	BWS (MPa)
Mine A	14.94	7.64	6.39	53.8	1.190	20.96
(This study)	12.83	9.53	8.69	32.3	1.099	23.97
	13.98	8.56	7.70	37.2	1.087	22.55
	15.5	11.98	8.50	16.4	1.029	39.06
	12.94	8.98	8.36	33.8	1.151	22.15
	27.4	16.26	9.86	44.8	1.269	36.29
	12.94	8.98	8.37	37.5	1.155	22.97
	12.94	8.98	8.38	36.9	1.143	23.11
	13.01	8.27	8.83	51.6	1.214	21.67
	13.55	8.77	8.26	53.0	1.206	16.99
	14.08	8.7	8.19	23.8	1.069	27.61
	14.08	8.7	8.19	33.7	1.118	24.13
	12.94	8.98	8.32	47.7	1.204	18.37
	17.74	13.86	8.71	30.0	1.102	30.10
	10.97	6.85	8.08	28.8	1.064	20.67
	13.72	7.7	8.32	52.0	1.272	20.03
	14.93	10.85	8.88	41.7	1.155	25.78
	14.93	10.85	8.89	22.5	1.043	29.06
	12.42	9.03	8.57	34.2	1.106	21.85
	15.99	12.5	9.27	56.3	1.253	22.67
	14.25	10.45	9.34	39.2	1.185	25.30
	14.25	10.45	9.36	43.2	1.188	23.97
	14.25	10.45	9.37	31.3	1.099	30.08
	14.25	10.45	9.40	35.4	1.143	26.21
	27.4	16.26	9.82	31.2	1.066	47.92
	18.36	12.44	9.50	38.8	1.116	28.05
	14.01	11.98	9.01	35.8	1.147	23.38
	14.93	10.85	8.85	18.8	1.073	28.86
	14.93	10.85	8.87	17.5	1.047	30.93
	14.93	10.85	8.91	45.7	1.228	21.67
	13.98	8.56	7.61	58.4	1.320	19.19
	22.88	15.06	10.69	51.4	1.185	31.69
	11	8.5	8.86	28.0	1.111	23.92
	14.93	10.85	8.94	30.9	1.029	28.62
(Xiang *et al*., 2024a)	13.55	8.77	8.32	45	1.22	22.83
	12.42	9.03	8.54	30.2	1.11	22.15
	27.4	16.26	10.08	27.35	1.09	55.36
(Martin, 1997)	60	11	45	48	1.14	120
(Lin *et al*., 2020a)	13.74	10.66	6.78	19.84	1.23	18.2
	10.15	7.39	6.9	14.17	1.21	17.61
(LeRiche, 2017)	72.6	37.95	35.7	42	1.14	102.2
	73.85	49.2	39.65	30	1.12	112
	67.09	49.49	41.21	42	1.18	136.94
	70.85	47	34.9	27	1.16	140

Appendix B: Comparison of the proposed model with the model developed by Lin *et al.* (2020c)

Fig. B1 and Table B1 present a comparison of estimation results and accuracies between the proposed model and the model developed by Lin *et al*. (2020c).
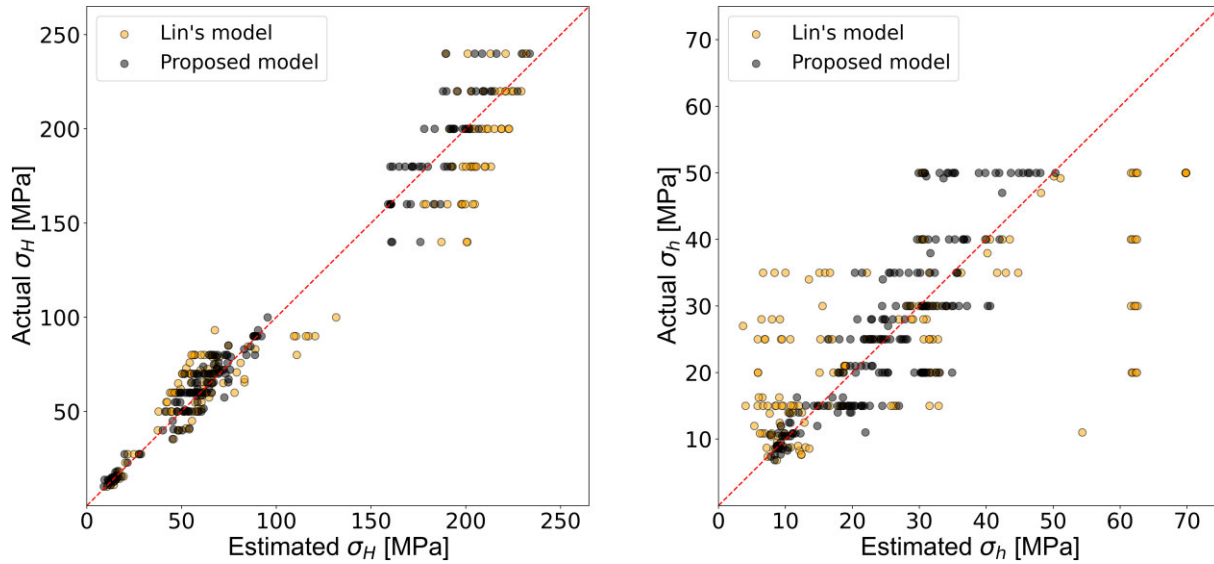
Figure B1. Comparison of horizontal stress estimation results between the proposed model and Lin's model.

Table B1. Comparison of estimation accuracies of σ_H and σ_h between the proposed model and Lin's model.

	Proposed model		Lin's model	
	MAPE (%)	RMSE (MPa)	MAPE (%)	RMSE (MPa)
σ_H	7.86	10.24	13.76	17.00
σ_h	18.99	6.627	38.53	13.37